Spectroscopic ultrahigh-resolution full-field optical coherence microscopy

Arnaud Dubois,[1,*] Julien Moreau,[1] and Claude Boccara[2]

[1]*Laboratoire Charles Fabry de l'Institut d'Optique, CNRS UMR 8501, Université Paris-Sud,
Campus Polytechnique, RD 128, 91127 Palaiseau, France*
[2]*Laboratoire d'Optique Physique, École Supérieure de Physique et Chimie Industrielles
CNRS UPR A0005, 10 rue Vauquelin, 75231 Paris Cedex 5, France*
*Corresponding author: arnaud.dubois@institutoptique.fr

Abstract: We have developed a full-field optical coherence microscopy system providing intensity-based tomographic images and spectroscopic information with ultrahigh spatial resolution. Local measurements of the backscattered light spectrum center of mass are achieved through short-time Fourier analysis of a stack of *en face* interferometric images acquired with a Linnik-type microscope. Using a halogen lamp as an illumination source enables us to achieve spectroscopic imaging over a wavelength range from 600 to 900 nm with a spatial resolution of ~ 1 µm. Absorption measurements of a colored gel are reported as a validation of the technique. Enhancement of tissue imaging contrast is demonstrated by imaging a *Xenopus Laevis* (African frog) tadpole *ex vivo.*

OCIS codes: (170.4500) optical coherence tomography; (170.3880) medical and biological imaging; (180.3170) interference microscopy; (170.6510) spectroscopy.

References and links

1. L. Vabre, A. Dubois, and A. C. Boccara, "Thermal-light full-field optical coherence tomography," Opt. Lett. **27**, 530-533 (2002).
2. A. Dubois, K. Grieve, G. Moneron, R. Lecaque, L. Vabre, and A. C. Boccara, "Ultrahigh-resolution full-field optical coherence tomography," Appl. Opt. **43**, 2874 (2004).
3. A. Dubois, G. Moneron, and A. C. Boccara, "Thermal-light full-field optical coherence tomography in the 1.2 µm wavelength region," Opt. Commun. **266**, 738-743 (2006).
4. K. Grieve, M. Paques, A. Dubois, J. Sahel, A.C. Boccara, J. F. Le Gargasson, "Ocular tissue imaging using ultrahigh-resolution full-field optical coherence tomography," Invest. Ophthalmol. Visual Sci. **45**, 4126-4131 (2004).
5. D. Huang, E. A. Swanson, C. P. Lin, J. S. Schuman, W. G. Stinson, W. Chang, M. R. Hee, T. Flotte, K. Gregory, C. A. Puliafito, and J. G. Fujimoto, "Optical Coherence Tomography," Science **254**, 1178 (1991).
6. J. G. Fujimoto, M. E. Brezinski, G. J. Tearney, S. A. Boppart, B. E. Bouma, M. R. Hee, J. F. Southern, and E. A. Swanson, "Optical biopsy and imaging using optical coherence tomography," Nature Med. **1**, 970 (1995).
7. A. F. Fercher, "Optical coherence tomography," J. Biomed. Opt. **1**, 157 (1996).
8. G. Moneron, A. C. Boccara, and A. Dubois, "Stroboscopic ultrahigh-resolution full-field optical coherence tomography," Opt. Lett. **30**, 1351-1353 (2005).
9. K. Grieve, A. Dubois, M. Simonutti, M. Paques, J. Sahel, J. F. Le Gargasson, A. C. Boccara, "In vivo anterior segment imaging in the rat eye with high speed white light full-field optical coherence tomography," Opt. Express **13**, 6286-6295 (2005).
10. M. D. Kulkarni and J. A. Izatt, CLEO '96. Summaries of Papers Presented at the Conference on Lasers and Electro Optics **9** (96CH35899) 59-60 (1996).
11. U. Morgner, W. Drexler, F. X. Kärtner, X. D. Li, C. Pitris, E. P. Ippen, and J. G. Fujimoto, "Spectroscopic optical coherence tomography, Opt. Lett. **25**, 111-113 (2000).
12. R. Leitgeb, M. Wojtkowski, A. Kowalczyk, C. K. Hitzenberger, M. Sticker, and A. F. Fercher, "Spectral measurement of absorption by spectroscopic frequency-domain optical coherence tomography," Opt. Lett. **25**, 820-822 (2000).
13. K. G. Larkin, "Efficient nonlinear algorithm for envelope detection in white light interferometry," J. Opt. Soc. Am. A **13**, 832-843 (1996).
14. D. Adler, T. Ko, P. Herz, and J. Fujimoto, "Optical coherence tomography contrast enhancement using spectroscopic analysis with spectral autocorrelation," Opt. Express **12**, 5487-5501 (2004).

15. B. Hermann, K. Bizheva, A. Unterhuber, B. Považay, H. Sattmann, L. Schmetterer, A. Fercher, and W. Drexler, "Precision of extracting absorption profiles from weakly scattering media with spectroscopic time-domain optical coherence tomography," Opt. Express **12**, 1677-1688 (2004).
16. C. Xu, P. Carney, and S. Boppart, "Wavelength-dependent scattering in spectroscopic optical coherence tomography," Opt. Express **13**, 5450-5462 (2005).
17. C. Xu, D. Marks, M. Do, and S. Boppart, "Separation of absorption and scattering profiles in spectroscopic optical coherence tomography using a least-squares algorithm," Opt. Express **12**, 4790-4803 (2004).
18. H. C. Van de Hulst, *Light scattering by small particles*, (Wiley, New York, 1957)
19. A. Dubois, L. Selb, L. Vabre, and A. C. Boccara, "Phase measurements with wide-aperture interferometers," Appl. Opt. **39**, 2326-2331 (2000)
20. A. Dubois, "Effects of phase change on reflection in phase-measuring interference microscopy," Appl. Opt. **43**, 1503-1507 (2004)
21. C. Xu, C. Vinegoni, T. S. Ralston, W. Luo, W. Tan, and S. A. Boppart, "Spectroscopic spectral-domain optical coherence microscopy," Opt. Lett. **31**, 1079-1081 (2006)
22. D. J. Faber, E. G. Mik, M. C. G. Alders, and T. G. van Leeuwen, "Light absorption of (oxy-)hemoglobin assessed by spectroscopic optical coherence tomography," Opt. Lett. **28**, 1437-1439 (2003)
23. C. Xu, J. Ye, D. L. Marks, and S. A. Boppart, "Near-infrared dyes as contrast-enhancing agents for spectroscopic optical coherence tomography," Opt. Lett. **29,** 1647-1649 (2004)
24. G. P. Delacretaz, R. W. Steiner, L. O. Svaasand, H. J. Albrecht, and T. H. Meier, "Epidermal melanin absorption in human skin," in Laser-Tissue Interaction and Tissue Optics, Proc. SPIE **2624**, 143-154 (1996).

1. Introduction

Full-Field Optical Coherence Microscopy (FF-OCM), also referred to as Full-Field Optical Coherence Tomography (FF-OCT), is an efficient technique for ultrahigh-resolution (~1 μm) three-dimensional imaging of biological media [1-4]. FF-OCM was proposed recently as an alternative method to conventional Optical Coherence Tomography (OCT) [5-7]. It uses a CCD camera as an array detector in combination with a spatially and temporally incoherent illumination source for parallel acquisition of *en face*-oriented (transverse) tomographic images. High detection sensitivity (> 90 dB) can be achieved through the accumulation of multiple images, which is permitted when *ex vivo* and hence immobile samples are imaged. *In vivo* full-field OCT imaging is possible with reduced detection sensitivity [8,9].

Spectroscopic OCT is an extension of conventional scanning OCT that is used for performing cross-sectional tomographic imaging and spectroscopic imaging simultaneously [10-12]. Information on the spectral content of backscattered light is obtained by detection and processing of the OCT interferometric signal. This method allows the spectrum of backscattered light to be measured over the entire available optical bandwidth, which can extend from 650 nm to 1000 nm using ultrabroad-band Ti:saphire laser technology [11].

Conventional spectrometer systems use a tungsten halogen lamp because of the extremely broad and smooth spectrum of thermal light. Since the usual illumination source of FF-OCM is also a tungsten halogen lamp, the combination of spectroscopy and FF-OCM seemed particularly appropriate. In this paper we present spectroscopic FF-OCM, an extension of the FF-OCM technique that is capable of providing spatially-resolved spectroscopic information with ultrahigh spatial resolution. Absorption measurements with spectroscopic FF-OCM are reported as a validation of the technique. Enhancement of tissue imaging contrast is demonstrated by imaging a *Xenopus Laevis* (African frog) tadpole *ex vivo*.

2. Spectroscopic FF-OCM: method

2.1 Experimental setup

The experimental setup of spectroscopic FF-OCM is represented schematically in Fig. 1. It is based on an interference microscope in the Linnik configuration, i.e., a bulk Michelson interferometer with identical microscope objectives - Olympus, 10x/0.3 W - in both arms. A Köhler halogen illuminator with a stabilized DC power supply is used as a spatially and temporally incoherent light source. The polished surface of an $Y_3Al_5O_{12}$ (YAG) crystal is placed at the focal plane of the microscope objective in the reference arm. Since water-immersion microscope objectives are used, the water/crystal interface constitutes a reference mirror with ~ 2% reflectivity. The object to be imaged is placed in the other arm of the interferometer under an identical water-immersion microscope objective. Identical glass plates

are placed in both arms of the interferometer. By adjusting the tilt of one of the plates, we can compensate for dispersion mismatch induced by the microscope objectives and the beam splitter. The plates are not tilted while the imaging depth in the imaged biological sample is varied. The numerical aperture of the microscope objectives is 0.3, providing a theoretical transverse (x-y) resolution of ~ 1.4 µm at the mean wavelength $\lambda = 750$ nm. The image of the reference mirror and the image of the object are projected with an achromatic doublet lens (500 mm focal length) onto a CCD camera array where they interfere with each other. The CCD camera - DALSA 1M15 - has the following characteristics: frame rate $f_{CCD} = 15$ Hz, 12 bits digitization, and 1024×1024 pixels. The CCD operates with 2×2 pixel binning in order to increase the detection sensitivity. The effective number of pixels is consequently reduced to 512×512. The object can be translated along the optical axis (z) by a computer-controlled piezoelectric transducer (PZT) - Polytech Pi P725 - in steps Δz. At each step p, an adjustable number m of identical interferometric images are captured by the CCD and transferred to the host computer, which calculates their sum. The resulting image E_p is then written on the computer hard disk in 32 bit binary format. A stack of N interferometric images $E_{p=1,...,N}$ is thus recorded, which represents a three-dimensional data-set of 512×512×N elements. The full interferometric signal as a function of depth in the object is thus acquired simultaneously by each CCD pixel. Due to the spectral response of the CCD camera and the optical elements of the experimental setup, the useful wavelengths range from approximately 600 nm to 900 nm. The fringe period (in water) may therefore vary between 225 nm and 340 nm. The PZT step is adjusted to $\delta z = 35$ nm, which ensures the sampling of the interferometric signal to be several times above the Nyquist limit. The PZT is equipped with absolute-measuring, direct-metrology capacitive sensors to minimize errors and fluctuations in the nominal step value. Data acquisition, camera control and PZT control are performed by a Visual C++ windows application. After recording the full interferometric signal, we can extract both the intensity-based images from the fringe envelope and the spectral information from the fringe pattern through data post-processing.
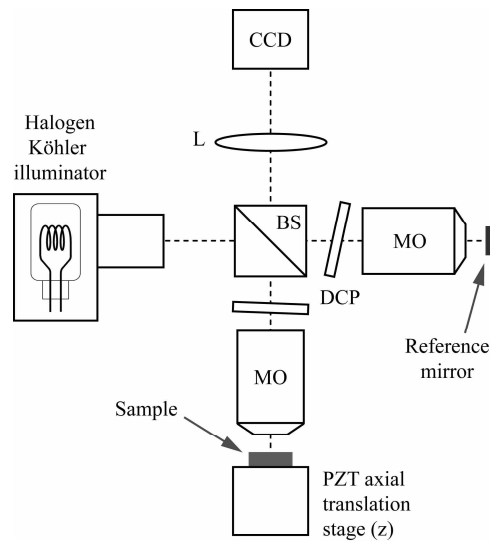

Fig. 1. Experimental arrangement of spectroscopic full-field optical coherence microscopy. BS: beam splitter (broadband, nonpolarizing), MO: microscope objectives (water-immersion, 10x, 0.3 NA), L: achromatic doublet lens (500 mm focal length). DCP: dispersion compensation plates. The object is translated in the axial direction in steps of 35 nm using a piezoelectric (PZT) translation stage. The reference mirror has a reflectivity of ~ 2%.

2.2 Intensity-based tomographic images

A stack of transverse-oriented (*x-y*) intensity-based tomographic images is obtained from the raw interferometric data by calculating the fringe envelope using a five-frame nonlinear phase-shifting algorithm [13]. Each intensity-based image I_k is calculated according to

$$I_k = \left(E_{k+2} - E_{k+6}\right)^2 - \left(E_k - E_{k+4}\right)\left(E_{k+4} - E_{k+8}\right), \quad k = 1,...,(N-8). \tag{1}$$

Because the mean wavelength is $\lambda = 750$ nm and the PZT step is $\delta z = 35$ nm, the adjacent frames in Eq. (1) are separated by a phase of $\sim \pi/2$ (considering the refractive index of the medium to be $n = 1.33$), as required in this phase-shifting algorithm. Each image I_k represents the transverse intensity distribution of light emanating from a thin slice orthogonal to the optical axis (*z*). The data-set $I_{(i,j,k)}$ of $512 \times 512 \times (N\text{-}8)$ elements is thus a three-dimensional image of the internal structures in the object which have backscattered the incident light. The imaging axial (*z*) resolution can be defined as the full width at half maximum (FWHM) of the fringe envelope along *z*, i.e., half the source coherence length, which is inversely proportional to the spectral bandwidth [7]. The axial resolution was measured to be 0.8 µm by imaging a silver mirror with a drop of water placed between the mirror and the objective. Since biological tissues consist mainly of water, the use of identical water-immersion microscope objectives in the two interferometer arms minimizes dispersion mismatch introduced by the tissues refractive index heterogeneities. The axial resolution degradation is thus minimized when the imaging depth increases.

Because the sampling step is $\delta z = 35$ nm, the fringe envelope along *z* is actually over-sampled. In order to benefit from all the acquired images, we reduce the intensity data-set $I_{(i,j,k)}$ to a matrix $I_{(i,j,k)}^*$ by summing 10 adjacent transverse tomographic images I_k. The compression of the data by a factor of 10 does not degrade the axial resolution. Tomographic images in arbitrary orientations, as well as image projections and volume rendering visualizations can then be produced from $I_{(i,j,k)}^*$. Calculations are performed in C programming language for maximum speed. Image production and processing are achieved using ImageJ and Matlab$^{\text{TM}}$ softwares.

High-resolution optical imaging of biological media requires a high detection sensitivity and a large dynamic range. These requirements in FF-OCM rely on several experimental parameters such as the reference mirror reflectivity and the full well capacity of the CCD pixels [2,3]. The full well capacity can be virtually increased by pixel binning and image accumulating. 2×2 binning is achieved by summing the signal delivered by 4 adjacent pixels. The image magnification on the CCD array is adjusted so that this binning does not reduce the transverse resolution. In order to keep the acquisition time relatively short, we choose to accumulate $m = 5$ raw images at each PZT step. As explained before, the three-dimensional intensity distribution $I_{(i,j,k)}$ is calculated by using a 5-frame phase-shifting algorithm, which means that each element of $I_{(i,j,k)}$ results from the combination of 5 accumulated images [according to Eq. (1)]. Finally, the compressed intensity distribution $I_{(i,j,k)}^*$ is the sum of 10 adjacent elements of $I_{(i,j,k)}$. With these conditions, the intensity detection sensitivity was measured to be ~ 85 dB.

2.3 Spectroscopic measurements

Spectroscopic information is obtained through Fourier analysis of the full interferometric signal recorded by each CCD pixel as a function of depth (*z*). Spatially-resolved power density spectra are calculated using a short-time Fourier transform. For each value of $1 \leq i, j \leq 512$ (each "binned" CCD pixel), "fast Fourier transforms" (FFTs) of the interferometric data (a vector of *N* elements) are calculated over a moving Gauss window. The

window is moved in steps of 10 points, so that a power density spectrum is associated with each element of the three-dimensional intensity data-set $I^*_{(i,j,k)}$.

The choice of the Gauss window size results in a trade-off between spectral resolution and spatial resolution of the spectral data. Our aim is to favor the spatial resolution. As a consequence, spectra will be measured with low spectral resolution. Only spectral shifts resulting from absorption within the tissues and backscattering by the sample microstructures will be measured. We chose a very narrow Gauss window, with width equal to the imaging axial resolution, i.e., a FWHM of 0.8 µm. The spectral impulse response of the system is the Fourier transform of this Gauss window. The spectral resolution, defined as the width (FWHM) of the spectral impulse response, is therefore equal to 240 nm. High spatial resolution of the spectral information is thus realized. Despite a low spectral resolution, high spectral sensitivity is achieved, which is required to measure weak spectral shifts. This point will be discussed later.

Before calculating the FFT, each data-set is increased in size to 4096 points by zero-padding in order to reduce the spectrum sampling step, which, after padding, is $\delta\sigma = \left(2 \times 4096 \times \delta z\right)^{-1} = 35$ cm^{-1} (~ 2 nm at $\lambda = 750$ nm). After a local spectrum has been calculated for each voxel of the three-dimensional intensity image $I^*_{(i,j,k)}$, it is necessary to quantify some aspect of the spectra for display. Due to our low spectral resolution, the measured spectra are always peak functions. As spectroscopic metric, we chose the spectrum center of mass.

For simultaneously displaying intensity and spectroscopic information, we use a HSL (hue, saturation, luminance) color map. Hue encodes the spectroscopic information (spectrum center of mass), whereas luminance and saturation together encode the intensity information, as done in [14]. We restrict the Hue variation from 0 to 0.5 (the full available hue range being from 0 to 1), so that the color varies from red to light blue (see color bar in Fig. 4). Luminance ranges from 0 to 1 and saturation from 0.5 to 1.

3. Interpretation of spectroscopic OCT measurements

Spectroscopic OCT is theoretically able to reveal spectral changes of light propagating in biological tissues due to elastic scattering and absorption. However, these two mechanisms are very different. Absorption takes place over the entire optical path, while scattering takes place at the local interfaces of refractive index inhomogeneities. In essence, absorption measurements are not truly spatially-resolved. In contrast, scattering measurements are more localized indicators. The contributions of both effects, however, are difficult to distinguish [15-17].

The spectral changes due to single-particle backscattering are related to the size of that particle [18]. In theory, spectroscopic OCT could be used in determining the size of scattering particles. In practice, the absolute determination of particle size by spectroscopic OCT is particularly difficult for several reasons:

* The wavelength-dependant attenuation of light due to absorption and scattering during the propagation from the sample surface to the imaged particle and back from the imaged particle to the sample surface.
* The presence of multiple scatterers in the coherence volume (the three-dimensional point-spread function) will generate interference, causing spectral modulations [14,16]. The number of scatterers in the coherence volume affects the spectral modulation. If the number of scatterers is large, the spectral modulation tends to be averaged out spatially. If the number of scatterers is small, dramatic modulation effects on the spectrum will occur. This situation is more likely to happen in high-resolution OCT, especially in FF-OCM where the coherence volume is ~ 1 µm^3. Even if the spectral modulations are not resolved by spectroscopic OCT (as is the case in our spectroscopic FF-OCM system), they may cause a spectral shift. Since it is often difficult to know whether one or several particles

are present in the coherence volume, it is difficult to be certain whether the measured spectral shift is a result of single-particle backscattering or multi-particle backscattering. Consequently, the determination of particle size is considerably hampered.

∗ The sample is not illuminated by a plane wave. Indeed the sample is illuminated with a distribution of incidence angles defined by the numerical aperture of the objective. This geometrical effect modifies the fringe period of the interferometric signal causing an apparent shift of the calculated spectrum. [16,19,20].

A few works have been published on wavelength-dependent scattering measurements achieved by spectroscopic OCT [16,17,21]. For the reasons cited above and due to the inhomogeneous properties of tissue scatterers, such as variations in size, refractive index, and density, the quantitative interpretation of scattering effects detected by spectroscopic OCT is still a challenge.

In contrast, a larger number of studies have focused on measuring the wavelength-dependent absorption from either endogenous or exogenous absorbers [15,22,23]. According to Beer's law, for an absorber to significantly shift the spectrum of backscattered light, the absorber either needs to have a large absorption cross-section, be present in high concentration or the length of the absorber region needs to be large. In order to maximize the imaging penetration depth, OCT uses near-infrared light where the absorption of biological tissues is minimal (so-called therapeutic window). Except for a few biological constituants such as melanin and blood (absorption peak of deoxy-hemoglobin at 760 nm and the haemoglobin isosbestic point at around 800 nm), endogeneous biological molecules have a very weak absorption cross-section in this spectral region. Finally, since OCT images structures at a typical depth between 0 and 1-2 mm, the effect of absorption is integrated over a small optical path. Consequently, the spectral modifications are generally faint.

4. Validation of the technique by absorption measurements

In order to validate spectroscopic measurements achieved by FF-OCM, we imaged the surface of a microscope slide (glass plate) covered by a layer of colored Agarose gel as depicted in Fig. 2 left. A microscope cover-slip was placed on top of the gel at an angle such that the gel acts as a wedge-shaped absorbing medium. The coloration was obtained by introducing blue ink during the gel preparation before solidification. The dispersion introduced by the microscope cover-slip was compensated for by placing an identical cover-slip in the other arm of the interferometer between the microscope objective and the beam splitter. A typical transmission spectrum of the ink (contained in a 1 mm thick glass cell), measured by a conventional grating-based spectrometer, is shown Fig. 2 right. Since the effective illumination spectrum of FF-OCM spreads from 600 nm to 900 nm, the absorption of the blue ink is expected to induce measurable spectral changes. Values of the spectrum center of mass shift measured with FF-OCM as a function of wedge thickness are reported in Fig. 3. As expected, the spectrum of the reflected light is shifted towards longer wavelengths at positions where the wedge is thicker.
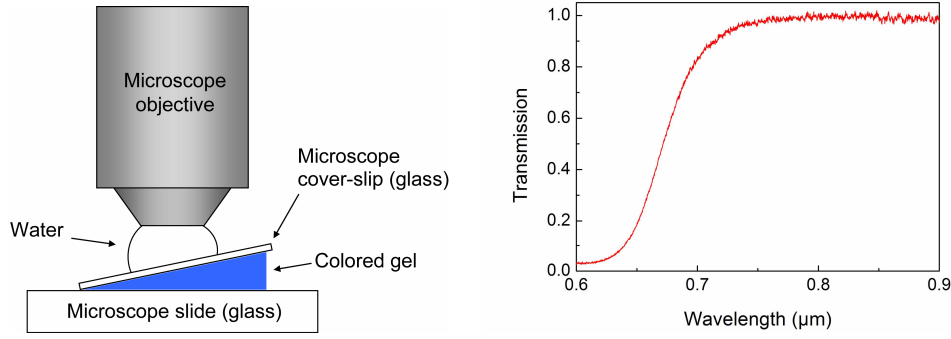
Fig. 2. Left: experimental arrangement for absorption measurement validation using spectroscopic FF-OCM. An Agarose gel colored with blue ink is placed between a microscope slide and a cover-slip. The wedge-shaped gel acts as an absorbing medium with variable thickness. Right: typical transmission spectrum of the blue ink measured by conventional spectrometry.

The theoretical shift was calculated assuming a Gaussian illumination spectrum $S_{illum}(\lambda)$ centered at $\lambda_0 = 750$ nm with width (FWHM) of 240 nm. After passing twice through the gel, the spectrum of light is then

$$S(\lambda) = S_{illum}(\lambda) \times T_{z,c}^2(\lambda) , \tag{2}$$

where

$$T_{z,c}(\lambda) = \exp\left[-\varepsilon(\lambda) zc\right] . \tag{3}$$

$\varepsilon(\lambda)$ represents the molar absorptivity of the ink, c the concentration of the ink, and z the thickness of the gel. The spectral transmission of the gel, $T_{z,c}(\lambda)$, can be deduced from the measured spectral transmission of the ink, $T_{z_0,c_0}(\lambda)$, shown in Fig. 2 right (glass cell of thickness z_0, ink concentration c_0):

$$T_{z,c}(\lambda) = \exp\left\{Kz \ln\left[T_{z_0,c_0}(\lambda)\right]\right\} \tag{4}$$

where

$$K = \frac{c}{z_0 c_0} . \tag{5}$$

The shift of the spectrum center of mass is then calculated as:

$$\delta\lambda = \frac{\int_0^\infty \lambda S(\lambda) d\lambda}{\int_0^\infty S(\lambda) d\lambda} - \lambda_0 . \tag{6}$$

By adjusting the value of the parameter K, the theoretical spectral shift $\delta\lambda$ (blue plot in Fig. 3) fits the experimental data (red plot in Fig. 3).

The RMS noise in the plot shown in Fig. 3 is an indicator of the sensitivity for spectral shift measurements. We estimate the sensitivity to be ~ 5 nm, which corresponds to the PZT nominal step fluctuations. This estimation is based on the reflection from a glass plate covered

with a gel, i.e. a reflectivity of ~ 0.35%, which is higher than the reflectivity of most biological structures. The spectral sensitivity when imaging biological tissues is degraded due to a lower signal-to-noise ratio. In the image presented in Fig. 4(B), for example, the spectral sensitivity varies from one point to another, depending on the intensity of the detected signal. The average spectral sensitivity over this entire image was measured to be ~ 20 nm. Melanocytes (indicated by white arrows) are the most backscattering structures; the spectral sensitivity in these regions was estimated to be ~ 10 nm.
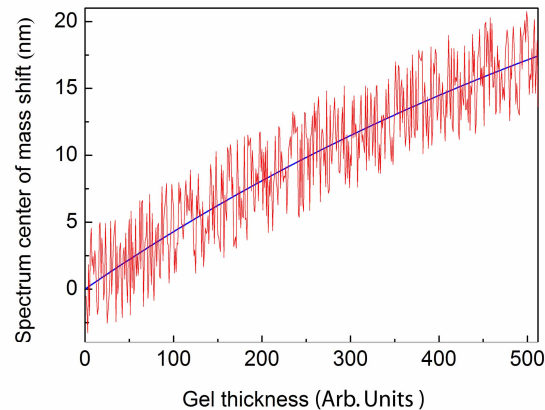

Fig. 3. Spectroscopic FF-OCM measurement (red) and calculation (blue) of the spectrum center of mass shift of light reflected by a glass plate after passing twice through an Agarose gel colored with blue ink (experiment depicted in Fig. 2). The scale factor of the x-axis is included in the fitting parameter K [see Eq. (4)].

5. Demonstration of imaging contrast enhancement

In order to illustrate the system's performances in imaging biological media, we imaged a *Xenopus Laevis* tadpole (*ex-vivo*). The tadpole was placed in a tank filled with phosphate-buffered saline (PBS, pH 7) for animal preservation and to provide index matching. A stack of N = 5000 images was recorded, which represents a three-dimensional data-set of 512×512×5000 elements (5 GigaBytes). The physical size of the imaged volume is 530µm×530µm×175µm (x×y×z). A vertical (x-z) tomographic image extracted from the three-dimensional data-set is shown in Fig. 4 with intensity-based contrast (A) and combined spectroscopic/intensity-based contrast (B).
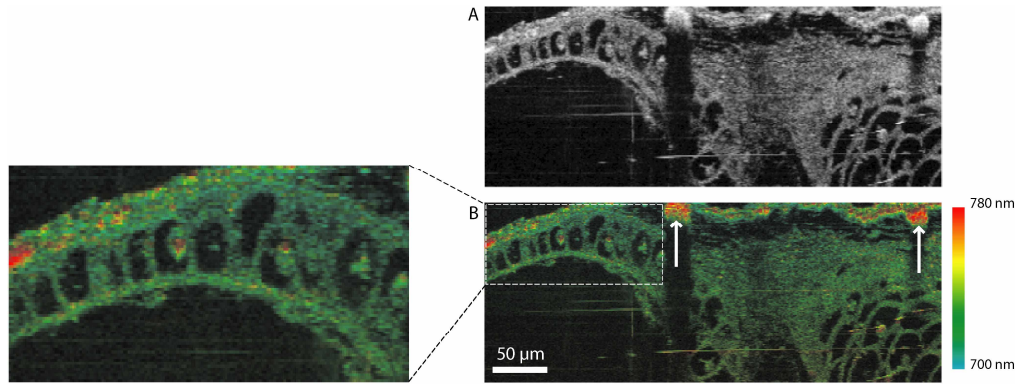
Fig. 4. Intensity (A) and combined intensity/spectroscopic (B) full-field optical coherence microscopy images of an *ex vivo Xenopus Laevis* tadpole embryo. The center of mass of the optical spectra is used as the spectroscopic metric. White arrows indicate the presence of melanocytes, more visible in the combined intensity/spectroscopic image due to a spectral shift of ~ 35 nm.

The intensity-based image [Fig. 4(A)], presented in logarithmic scale, reveals the internal tissue morphology. Pleomorphic mesenchymal cells can be visualized. Cell membranes, cell nuclei and melanocytes appear highly backscattering as compared to cytoplasm. Because of the large number of images acquired by the CCD, the calculated intensity-based images show very good contrast and exhibit a low noise level.

The same image with combined spectroscopic/intensity information is shown in Fig. 4(B). We point out the ultrahigh spatial resolution of the spectroscopic information displayed in this image. Melanocytes (see arrows) appear red with our colormap, indicating an average spectral shift of ~ 35 nm towards longer wavelengths as compared to the mean spectrum center of mass over the entire image. The possible physical mechanisms responsible for this spectral shift are scattering and absorption. Melanocytes are relatively strong light scatterers (see Fig. 4(A). According to Rayleigh's theory, the amount of scattering increases sharply as the wavelength of the light decreases. A blue-shift of the backscattered light spectrum would then happen, which is in contradiction with the observation. One possible explanation is that light scattering by the melanocytes is not described by Rayleigh theory, because the size of the scattering structures is not very small compared to the optical wavelength. However, even with Mie theory, scattering cannot explain the measured spectral shift. Below the melanocytes, a shadow is observed, which is due to a strong absorption of light by these biological structures. The absorption of melanin decreases monotonically with the wavelength in the visible and near infrared [11,24]. We think that absorption is therefore the predominant effect responsible for the spectral changes of light backscattered by the melanocytes. A "red" spectral shift immediately below the melanocytes is not observed because the transmission of light through theses biological structures is too weak. At sufficient depths, the shadow disappears because light is able to pass around the melanocytes due to the relatively high numerical aperture of the microscope objective (look at the small melanocyte on the right of the image). For this light, absorption has not occurred, and significant spectral changes are consequently not observed. Similar results have been reported with conventional spectroscopic OCT [11]. A slight red-shift of the measured spectra with increased imaging depth can be observed in the image. This tendency is consistent with the fact that longer wavelengths penetrate deeper than shorter wavelengths due to reduced scattering [11,14]. However, the imaging depth is not large enough here (175 µm) to make this phenomenon clearly visible.

The acquisition time of the three-dimensional data-set was $(1/f_{CCD}) \times m \times N + \tau \times N \sim 110$ min . This relatively long acquisition time was limited by the CCD frame rate f_{CCD} and the time $\tau \sim 1$ s spent accessing and writing the data on the computer

hard disk. The size of the acquired raw data-set is considerable ($\sim 10^9$ "points"). Because of the acquisition time, the technique is presently not appropriate for *in vivo* imaging. Nevertheless, as demonstrated here, it may be applicable in the biomedical domain on *ex vivo* or immobile samples.

6. Conclusion

In summary, we have developed a FF-OCM system capable of providing combined spectroscopic/intensity three-dimensional images. Spatially-resolved measurements of the spectrum of light backscattered by the sample are achieved through short-time Fourier analysis of a stack of *en face*-oriented interferometric images. Intensity images with ultrahigh spatial resolution (~ 0.8 µm $\times$ 1.4 µm, axial $\times$ transverse) are extracted from the interferometric image stack using a non-linear 5-frame image combination. Due to the broad and smooth spectrum of the illumination source (halogen lamp), spectroscopic imaging is possible over a wavelength range from 600 to 900 nm. The centers of mass of the low-resolution measured spectra are calculated to provide local spectroscopic information.

As a validation of the spectroscopic FF-OCM technique, we have carried out absorption measurements in a model sample (a colored Agarose gel). We have demonstrated that spectroscopic FF-OCM may enhance the contrast of biomedical imaging, making differentiation of distinct tissues easier. At the price of an increase of the acquisition time, spectroscopic FF-OCM may provide improved imaging compared to conventional FF-OCM.